

## Experimental study of nuclear fission along the thorium isotopic chain: From asymmetric to symmetric fission

A. Chatillon,<sup>1,\*</sup> J. Taïeb,<sup>1</sup> H. Alvarez-Pol,<sup>2</sup> L. Audouin,<sup>3</sup> Y. Ayyad,<sup>2,†</sup> G. Bélier,<sup>1</sup> J. Benlliure,<sup>2</sup> G. Boutoux,<sup>1</sup> M. Caamaño,<sup>2</sup> E. Casarejos,<sup>4</sup> D. Cortina-Gil,<sup>2</sup> A. Ebran,<sup>1</sup> F. Farget,<sup>5</sup> B. Fernández-Domínguez,<sup>2</sup> T. Gorbinet,<sup>1</sup> L. Grente,<sup>1</sup> A. Heinz,<sup>6</sup> H. T. Johansson,<sup>6</sup> B. Jurado,<sup>7</sup> A. Kelić-Heil,<sup>8</sup> N. Kurz,<sup>8</sup> B. Laurent,<sup>1</sup> J.-F. Martin,<sup>1</sup> C. Nociforo,<sup>8</sup> C. Paradela,<sup>2,‡</sup> E. Pellereau,<sup>1</sup> S. Pietri,<sup>8</sup> A. Prochazka,<sup>8</sup> J. L. Rodríguez-Sánchez,<sup>2,§</sup> H. Simon,<sup>8</sup> L. Tassan-Got,<sup>3</sup> J. Vargas,<sup>2,||</sup> B. Voss,<sup>8</sup> and H. Weick<sup>8</sup>

<sup>1</sup>CEA, DAM, DIF, F-91297 Arpajon, France

<sup>2</sup>IGFAE, Universidade de Santiago de Compostela, E-15782, Santiago de Compostela, Spain

<sup>3</sup>IPN Orsay, CNRS/IN2P3, Université Paris-Saclay, Université Paris-Sud, F-91406 Orsay, France

<sup>4</sup>Department of Mechanical Engineering, University of Vigo, E-36310 Vigo, Spain

<sup>5</sup>CNRS, GANIL, Bd H. Becquerel, 14076 Caen, France

<sup>6</sup>Department of Physics, Chalmers University of Technology, 41296 Gothenburg, Sweden

<sup>7</sup>CNRS, CENBG, F-33175 Gradignan, France

<sup>8</sup>GSI-Helmholtzzentrum für Schwerionenforschung GmbH, D-64291 Darmstadt, Germany



(Received 18 April 2019; published 30 May 2019)

The inverse kinematics technique, applied to radioactive beams and combined to the Coulomb excitation method, is a powerful tool to study low-energy fission. A novel experimental setup was developed within the R3B/SOFIA (Reactions with Relativistic Radioactive Beams/Studies On Fission with Aladin) collaboration to identify in mass and atomic numbers both fission fragments in coincidence. These new data provide elemental, isobaric, and isotonic yields for the fission along the thorium isotopic chain. Results are also compared to previous measurements using either the same reaction mechanism or thermal-neutron induced fission. This latter comparison permits to probe the influence of the excitation energy in the fission process.

DOI: [10.1103/PhysRevC.99.054628](https://doi.org/10.1103/PhysRevC.99.054628)

### I. INTRODUCTION

Fission permits to study the interplay of macroscopic and microscopic degrees of freedom in the nucleus in a unique way. At low excitation energies, this reaction mechanism is strongly influenced by nuclear structure. Shell and pairing effects play a major role in the shape of the mass and nuclear charge distributions of the fission fragments. However, the already available observables provide only indirect access to the influence of nuclear structure on the fission process. Therefore, additional experimental information is important for improving our understanding of this process.

Fission studies employing radioactive beams were a first key step that offered a number of experimental advantages. In contrast to fission studies based on stable or long-lived fissile targets that are irradiated by neutrons, photons, or light-charged particles, radioactive beams allow varying the proton

and neutron number of the fissioning system over a much wider range. An example is the pioneering fission studies with radioactive beams at relativistic energies in inverse kinematics that allowed for the first time, to map the transition from asymmetric fission in the actinides to symmetric fission in preactinide nuclei [1]. A different approach was exploited at ISOLDE, where asymmetric fission in  $\beta$ -delayed fission of  $^{180}\text{Hg}$  and neighboring nuclides was studied [2,3]. Note that the former experiment measured the fission-fragment nuclear charge distributions, while the latter studied the fission-fragment mass distributions.

Measuring the mass and the charge of both fission fragments simultaneously, especially for heavy charges and masses, represents a great challenge for experimental physics. In conventional experiments, a reasonable charge resolution is achievable only for the light fragments ( $Z \leq 42$ ) and even this requires a high-resolution spectrometer, or is limited to fission fragments of very high kinetic energies [4]. An additional limitation is the restriction to thermal-neutron-induced fission, since the fission cross section dramatically drops for increasing neutron energies. Another approach, using  $\gamma$ -ray spectroscopy of fission fragments, is not limited by the absolute value of  $A$  and  $Z$  of the fission fragments, but the determination of fission-fragments yields is complicated by the need of accurate branching ratios [5]. Recent progress in the study of fission of uranium up to californium, induced by transfer reactions, was performed with the VAMOS

\*audrey.chatillon@cea.fr

<sup>†</sup>Present address: National Superconducting Cyclotron Laboratory, Michigan State University, East Lansing, MI 48824-1321, USA.

<sup>‡</sup>Present address: EC-JRC, Institute for Reference Materials and Measurements, Retieseweg 111, B-2440 Geel, Belgium.

<sup>§</sup>Present address: GSI-Helmholtzzentrum für Schwerionenforschung GmbH, D-64291 Darmstadt, Germany.

<sup>||</sup>Present address: Universidad Santo Tomás, Tunja, Colombia.

spectrometer. These experiments allow for the identification of a wider range of fission fragments, but only one fission fragment at a time was measured in the spectrometer [6]. Therefore, data on fission fragments yields are, up to now, still incomplete despite decades of investigations. Such a lack of high-resolution data constitutes an obstacle for the development of reliable models. To overcome this longstanding problem, the R3B/SOFIA collaboration developed an experimental apparatus based on the idea of the pioneering experiment of Ref. [1], to detect both fission fragments produced by electromagnetic-induced fission of relativistic radioactive beams from preactinide up to neptunium nuclides, but pushing it a step further, since the setup permits to identify, in coincidence, both fission fragments in mass number  $A$  and atomic number  $Z$  [7–9].

The present paper reports on the study of the transition from the asymmetric to the symmetric fission along the thorium chain, which was first observed in Ref. [1]. We can therefore compare our results and complete them with the isobaric and isotonic yields. A final comparison is then made between our measurement of Coulomb-induced fission of  $^{230}\text{Th}$  and previous studies of thermal-neutron induced fission of  $^{229}\text{Th}$  [10,11]. These two reactions populate the same compound nucleus but at two different excitation energies.

## II. EXPERIMENTAL METHOD AND SETUP

As in the previous experiment [1], electromagnetically induced fission is studied using inverse kinematics at relativistic energies. At these energies, ions are mainly fully stripped. Thus the ionic charge ( $Q$ ), obtained from the energy-loss measurement, directly gives the nuclear charge ( $Z$ ). By combining this energy-loss measurement of the ion with its time of flight (ToF) and its tracking through a magnetic dipole ( $B\rho$ ), the mass ( $A$ ) of the ion can be deduced using the so-called  $\Delta E$ - $B\rho$ -ToF method, based on the equation:  $A/Z \propto B\rho/\beta\gamma$ , where  $\beta$  is the ratio of  $v$  to  $c$ , and  $\gamma$ , the Lorentz factor. The breakthrough of SOFIA, compared to previous experiments, is that the  $\Delta E$ - $B\rho$ -ToF method is applied at two levels, for the unambiguous identification of the secondary beam and of each fission fragment in coincidence.

For this purpose, the experiment can only take place at the GSI/FRS facility, the only heavy-ion accelerator to provide and identify secondary actinide beams at relativistic energies up to neptunium isotopes. Moreover, the experimental setup was conceived to fit the already existing ALADIN dipole (A Large Acceptance Dipole magNet, [12]), located in the GSI Cave C and mandatory to identify the mass numbers of both fission fragments.

### A. Secondary-beam production and identification

All secondary actinide beams were produced by fragmentation of a  $^{238}\text{U}$  primary beam at 1A GeV in a  $1036\text{ mg/cm}^2$  Be target mounted together with a  $223\text{ mg/cm}^2$  Nb stripper. The secondary beams are selected by the fragment separator (FRS [13]) operated as a momentum-loss achromatic spectrometer [14]. The dipoles provide two consecutive magnetic

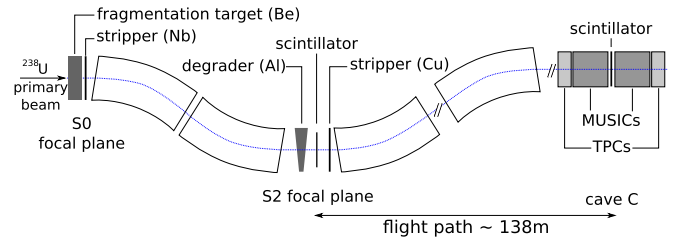


FIG. 1. Schematic view of the FRS and of the first part of the setup, dedicated to the identification of the secondary beams.

selections, from S0 to S2 and from S2 (intermediate focal plane of the FRS) to Cave C. A  $2200\text{ mg/cm}^2$  degrader was placed at S2. As previously mentioned, part of the experiment was dedicated to the study of the fission along the thorium isotopes chain. For this purpose, three FRS settings were applied, each of them lasted for 4 h, to produce cocktail beams centered around  $^{222,226,230}\text{Th}$ .

Figure 1 shows the part of our setup dedicated to the identification of the secondary beams. Event by event, the time of flight is measured on a 138 m long flight path, by two plastic scintillators located at S2 and at the entrance of Cave C. Both scintillators also provide horizontal position measurements, based on the time difference between two photomultipliers mounted on the left and right side of the scintillator. Two time-projection chambers (TPC [15]) and two multiple-sampling ionization chambers (MUSIC [16]), were mounted at Cave C to complete this setup. The angle of the incoming ion is obtained using both TPC detectors. Two independent measurements of the ionic charge states,  $Q_1$  and  $Q_2$ , are inferred from the energy-loss measurements given by the first and second MUSIC detectors.

Figure 2 represents the  $Q_1$  versus  $Q_2$  correlation plot. It clearly shows that at such energies, around 600A MeV in the MUSIC detectors, part of the actinides may not be fully stripped and can, in flight, pick up or lose one electron in the material on the flight path, as highlighted by the three

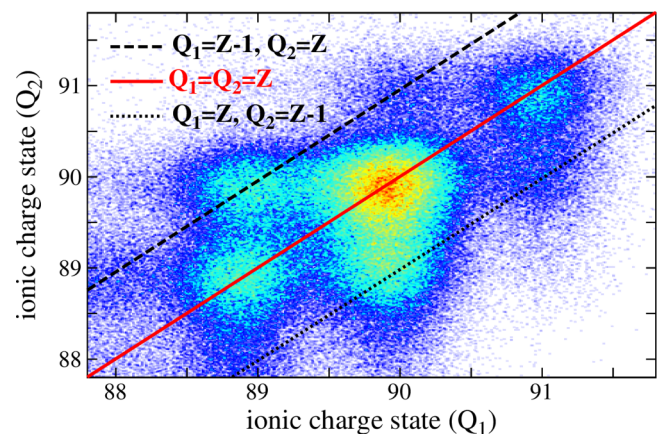


FIG. 2. Correlation plot between the two ionic charge-state measurements of the secondary beam, obtained from the FRS setting centered around  $^{226}\text{Th}$ . The three lines represent the three main combinations of charge states in both MUSIC detectors.

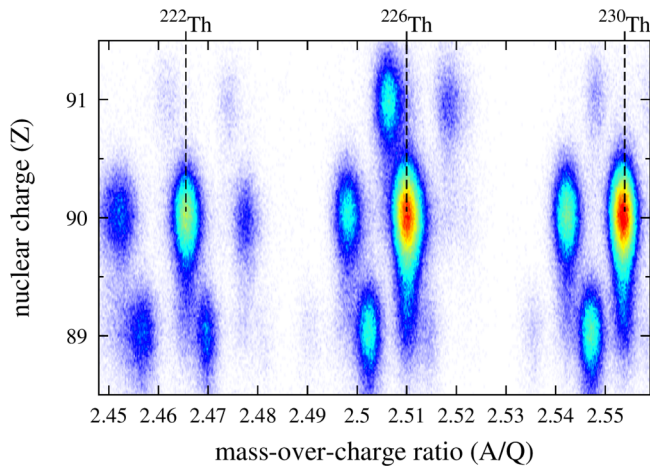


FIG. 3. Identification plot of the cocktail beams centered around  $^{222,226,230}\text{Th}$ . Only events leading to fission in the active target (anodes or cathodes) or in the exit window of the second MUSIC are selected. Other events are rejected by the trigger (if no fission occurs) or by the analysis.

guide lines. The central thick red line corresponds to events where the incoming beam is fully stripped in both detectors. The dashed (dotted) black line corresponds to events where the incoming beam has one electron in the first (second) MUSIC detector. Therefore, as soon as the heavy ion is measured fully stripped in one MUSIC ( $Q = Z$ ), the correct value of the nuclear charge is then assigned by taking the maximum of both measurement. Such a plot minimizes the misidentification of the nuclear charge of the actinides. However, the measurement of some events is still improper when the heavy ions are not fully stripped in both MUSIC detectors. Nevertheless, such events can be discriminated based on the correlation of the assigned nuclear charge with the mass-over-charge ratio obtained from the  $\Delta E$ - $B\rho$ -ToF method. This is illustrated in Fig. 3, which represents the identification plot of the secondary beams for all FRS settings. The nuclides are well separated, and exhibit a tail, corresponding to 12% of the events, toward one charge below the beam charge. This tail corresponds to the above-mentioned misidentified nuclear charge, where the beam was not fully stripped in both MUSIC detectors. Thanks to the resolution in  $A/Q$ , these events are well separated from the  $(Z - 1)$  compound nuclei. Therefore, each fissioning nucleus can be unambiguously selected on an event-by-event basis, from geometrical cuts.

### B. Fission reaction and excitation energy

Low-energy fission of the secondary radioactive beams is induced by Coulomb excitation using high- $Z$  targets (two uranium targets and one lead target) mounted as cathodes in an active target. The excitation energy cannot be measured in this experiment but is estimated. These estimations are based on the total electromagnetic differential cross section, using the mean beam energy in the center of the active target ( $\langle E \rangle_{MOT}$ ) calculated from LISE++ V.10.0.32 [17], and second, from the fission probability obtained using the general fission model (GEF, version 2019-1.1 [18]).

TABLE I. Cross sections and mean excitation energies for the  $(\gamma, \text{tot})$  and  $(\gamma, f)$  reactions, with the parametrization of  $^{232}\text{Th}$  GDR from [19].

beam	$\langle E \rangle_{MOT}$ [A MeV]	$\sigma(\gamma, \text{tot})$ [b]	$\langle E^* \rangle_{(\gamma, \text{tot})}$ [MeV]	$\sigma(\gamma, f)$ [b]	$\langle E^* \rangle_{(\gamma, f)}$ [MeV]
$^{219}\text{Ac}$	552.3	6.0	12.1	0.5	17.4
$^{220}\text{Ac}$	562.0	6.1	12.1	0.7	16.3
$^{223}\text{Ac}$	561.4	6.2	12.1	0.5	16.8
$^{227}\text{Ac}$	568.9	6.3	12.0	0.4	16.2
$^{221}\text{Th}$	564.5	6.1	12.1	4.6	13.4
$^{222}\text{Th}$	559.2	6.2	12.1	4.4	13.5
$^{223}\text{Th}$	555.8	6.1	12.1	4.5	13.5
$^{225}\text{Th}$	554.5	6.2	12.0	4.2	13.6
$^{226}\text{Th}$	556.5	6.3	12.0	3.7	13.8
$^{229}\text{Th}$	563.9	6.4	12.0	2.7	14.5
$^{230}\text{Th}$	564.4	6.4	12.0	2.0	14.9
$^{228}\text{Pa}$	551.7	6.3	12.0	5.4	12.9
$^{229}\text{Pa}$	552.5	6.4	12.0	5.1	13.1

In Coulomb interaction, giant dipole resonances (GDR) and giant quadrupole resonances (GQR) are typically excited. The total electromagnetic differential cross section is calculated, taking into account these two major components (GDR and GQR), following the calculation in Ref. [1] based on the hydrodynamic model. However, a study of the photofission cross section [19] performed on the  $^{232}\text{Th}$ ,  $^{235,236,238}\text{U}$  fissioning nuclei, still based on the hydrodynamic model, adopts modified GDR parameters, which reproduce better experimental data than the one based on the pure hydrodynamic model. In this work, both parametrizations (from the hydrodynamic model and from the  $^{232}\text{Th}$ -GDR parameters from [19]) were tested and compared. Figure 4(a,b,c,d) shows this comparison for the beams  $^{220}\text{Ac}$ ,  $^{222,226}\text{Th}$ , and  $^{228}\text{Pa}$ . In both cases, the total differential electromagnetic cross section is distributed with a mean excitation energy of about 12 MeV showing a tail up to 35 MeV, while the total electromagnetic cross section is roughly 6 b. Figure 4(e,f,g,h) shows the fission probability obtained from the GEF model [18]. Each strong increase of the fission probability corresponds to the opening of a higher fission chance, except for the first peak in the thorium and protactinium isotopes. For these nuclides (f,g,h), the fission barrier ( $B_f$ ) is lower than the neutron separation energy ( $S_n$ ). Above  $S_n$ , neutron emission competes with fission, leading to a strong decrease of the fission probability. Finally, Fig. 4(i,j,k,l) shows the calculated excitation functions. The mean values of the excitation energy and the integrated cross sections for the full set of incoming beams are given in Table I. These mean values depend on the fission probability, which is not well understood since the fission barriers of those exotic nuclei are not precisely known. This implies that the values given in the last column of Table I are not precise and we estimate that they have an uncertainty of 0.5 MeV.

In competition with the Coulomb-excitation mechanism, projectile fragmentation can occur for smaller impact parameters. The pre-fragment produced after the initial fragmentation stage may de-excite through fission and will be detected in

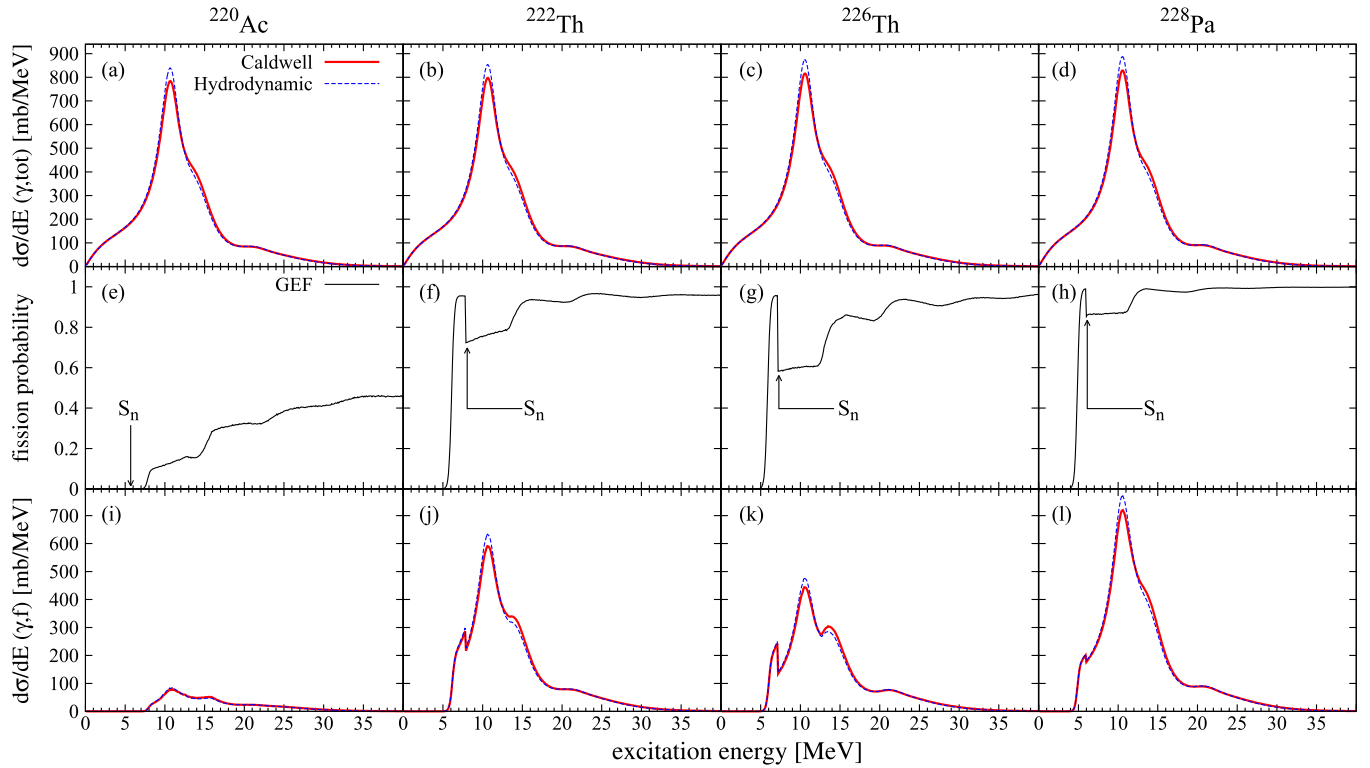


FIG. 4. The total electromagnetic differential cross section (first row), the fission probability (second row), and the excitation function (third row) are plotted as function of the excitation energy for the following fissioning nuclei:  $^{220}\text{Ac}$  (first column),  $^{222}\text{Th}$  (second column),  $^{226}\text{Th}$  (third column), and  $^{228}\text{Pa}$  (fourth column). The total electromagnetic differential cross sections are calculated for a beam at the energy  $(E)_{\text{MOT}}$  given in Table I on a  $^{238}\text{U}$  target with the parametrizations, from [19] (red full line), and from the hydrodynamic model (blue dashed line). The fission probabilities are calculated by GEF. The neutron separation energy ( $S_n$ ) is indicated by an arrow.

our setup. This fragmentation-fission component is removed from our data during the analysis. In the first step, only events where the sum of both fission-fragments nuclear charges ( $Z_{\text{sum}}$ ) is equal to the nuclear charge of the fissioning nucleus ( $Z_{\text{CN}}$ ), are analyzed. Yet, a nuclear reaction component remains, originating from fission after fragmentation reaction where no protons are removed. This component cannot be removed on an event-by-event basis, but can be subtracted using data on fission in light- $Z$  materials. For this purpose, fission events in layers of aluminium (anodes of the active target) and glass (exit window of the second TUM-MUSIC) are selected. The contribution of this last fragmentation-fission component is given in Table II of Appendix B. The full subtraction procedure is described and illustrated in Ref. [8].

### C. Fission-fragment identification

The setup for the isotopic identification of both fission fragments is represented in Fig. 5. Fission takes place in the active target. Fission fragments are emitted at forward angles and go through a twin-MUSIC made of two identical MUSIC detectors with a common vertical cathode. Each part has a segmented anode plane in order to derive for each fission fragment its nuclear charge (directly from the energy-loss signals, since contrary to actinides, fission fragments are fully stripped) and its horizontal angle (from the electrons drift times). To complete the tracking, two multi-wire proportional

chambers (MWPC, [20]) located up- and downstream from ALADIN provide the  $(x, y)$  coordinates. Finally the time of flight of each fragment is measured between the plastic scintillator, and the time-of-flight wall [21]. Compared to Ref. [8], the setup is the same except for the gas used in the twin-MUSIC. Indeed, after a few days of beam time, the twin-MUSIC exhibited some discharge events, which prevented us from working at the nominal value of the electric field in the detector. The Ne-based gas mixture (84.7% Ne, 12%  $\text{CH}_4$ , 3%  $\text{CO}_2$ , and 0.3%  $\text{N}_2$ ) was replaced with P25 gas (25%  $\text{CH}_4$  and 75% Ar). It allowed the twin-MUSIC to work at a lower voltage, but strongly degraded the mass resolution, mainly due to the increased angular straggling in argon.

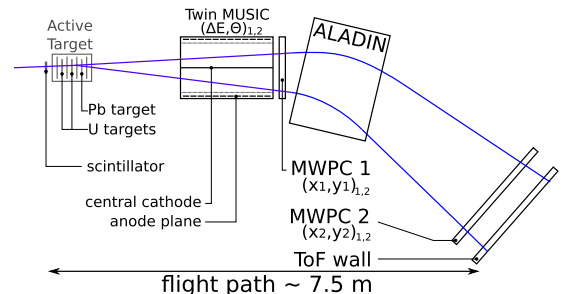


FIG. 5. Schematic view of the R3B/SOFIA setup dedicated to the identification of both fission fragments in coincidence.

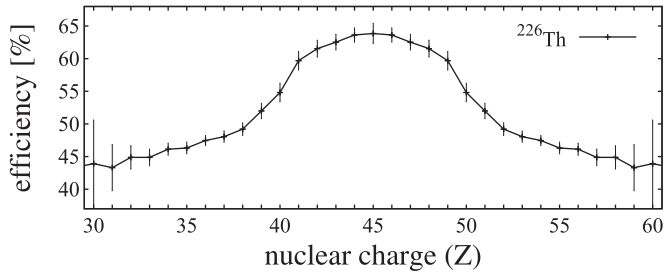


FIG. 6. Variation of the efficiency with the nuclear charge. Error bars originate from the statistical uncertainty of the data.

### III. ANALYSIS

#### A. Efficiency correction

The results need to be corrected for the efficiency of the experimental setup. The latter was determined by a full Monte Carlo simulation, based on the COde for simulating experiments on Nuclear FISSION using a large Dipole (CONFID, [22]), using GEF [18] as event generator. The simulation is validated by the data, especially by the  $(x, y)$  position distributions for each  $Z$  in the MWPC detectors. Figure 6 shows one example of the variation of the efficiency as a function of the nuclear charge of the fission fragments. As explained in Ref. [8], several sources of efficiency loss were identified: first, if both fission fragments were passing through the same half of the twin-MUSIC; second, if one fission fragment was crossing the central cathode. Such events were eliminated from the analysis. However, the plastics of the time-of-flight wall exhibited a light-attenuation length that was shorter than expected, and some photomultiplier tubes had a lower nominal high-voltage value. As a consequence, events characterized by a very asymmetric fission with a light fragment hitting the edge of the plastic were partially lost. It leads to a loss of efficiency for asymmetric splitting (see Fig. 6). This explains why the efficiency, given in Table II of Appendix B, increases for fissioning isotopes favoring symmetric fission.

#### B. Fission distributions

The energy loss is measured for each fission fragment in the twin-MUSIC before conversion into nuclear charge (see [8] for details on the analysis method). Figure 7 shows the elemental distributions for Coulomb-excitation induced fission in  $^{226}\text{Th}(\gamma, f)$ .

By combining the nuclear charge with the measurements of the velocity and bending radius in ALADIN, the mass of each fragment can be extracted. Figure 8 shows the distribution for the mass and the neutron number obtained from the electromagnetic fission of the most populated thorium isotope ( $^{226}\text{Th}$ ). Compared to the mass resolution obtained in Ref. [8], due to the additional straggling introduced by the heavier gas mixture, the mass resolution is degraded for the light fragments and lost for the heavier ones.

A summary of the statistics of the different physics cases can be found in Table II in Appendix B and the distribution for all nuclides in Figs. 16, 18, and 19 of Appendix A. As can

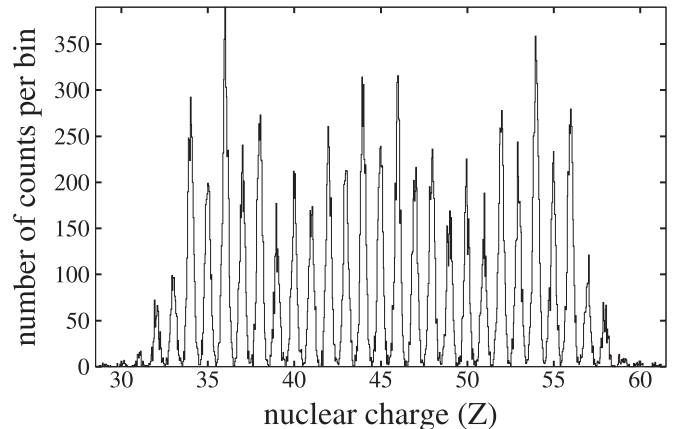


FIG. 7. Elemental distributions measured for  $^{226}\text{Th}(\gamma, f)$ .

be seen in Figs. 18(g) and 19(g), the setting centered around  $^{230}\text{Th}$  is slightly worse with respect to the mass resolution. Indeed, the latter setting was the first with the new gas mixture, and even though the twin-MUSIC had been flushed for a few hours, the gas was not fully purified. During this setting, its properties (mainly energy loss and drift velocity of the electrons) were still changing.

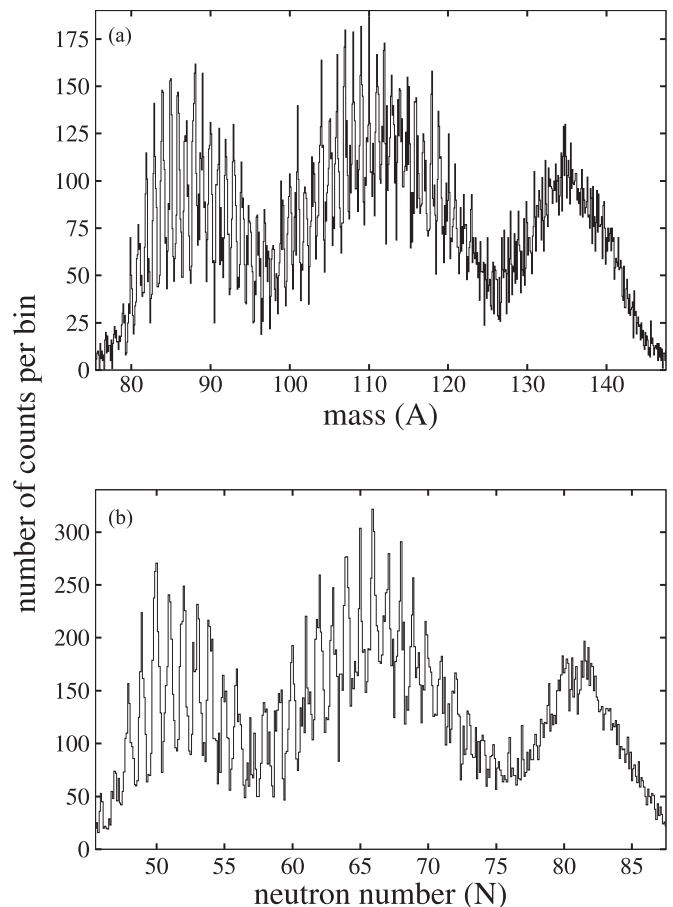


FIG. 8. Isobaric (a) and isotopic (b) distributions measured for  $^{226}\text{Th}(\gamma, f)$ .

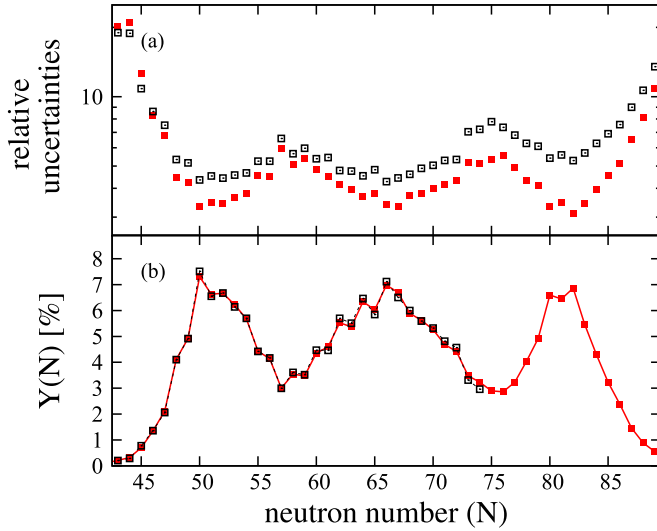


FIG. 9. Illustration of the analysis to infer the isotonic yields from the electromagnetically induced fission of the  $^{226}\text{Th}$ . Rebinned data, normalized to 200% are represented in red. Results from the multi-Gaussian fit in black. (a) relative uncertainties: the red full squares represent the statistical, whereas the black open squares the systematic extracted from the fit. (b) Isotonic yields.

### C. Extraction of the yields

The final elemental distributions (shown in Fig. 16) are characterized by well-separated peaks for the different nuclear charges. Therefore, the elemental yields  $Y(Z)$  are calculated by integrating those distributions for each charge. The yields are then normalized so that their sum is equal to 200%.

From the isotonic and isobaric distributions a multi-Gaussian fit is performed on the resolved part of the spectra. This fit procedure is done iteratively, until the width of each Gaussian adopts a smooth variation with respect to the mean values. Figure 9 illustrates, with the black open squares, the result of such a procedure for  $^{226}\text{Th}(\gamma, f)$ . In the same figure, the red full squares represent a first approximation of isotonic yields. They are obtained by summing all counts with values between  $N - 0.5$  and  $N + 0.5$  and are finally normalized to 200%. The agreement is excellent, thus for the unresolved part of the distribution, the yields are taken from this first approximation, but they have a larger systematic uncertainty. For the resolved part, the systematic uncertainties are extracted from the fit, whereas for the unresolved part they are estimated, taking into account the resolution loss. Finally, isotonic and isobaric yields could be extracted for the following fissioning nuclei:  $^{221,222,225,226,229,230}\text{Th}$  and  $^{228}\text{Pa}$ . The lack of statistics for the other fissioning nuclei prevents obtaining results with a reasonable level of uncertainty.

## IV. RESULTS

### A. Elemental yields

In Fig. 10, our data (in red full line) are shown for the three most populated secondary beams ( $^{222,226,230}\text{Th}$ ) and compared with Ref. [1] (in blue dashed line). The agreement between both data sets is excellent. Nevertheless, slight differences are

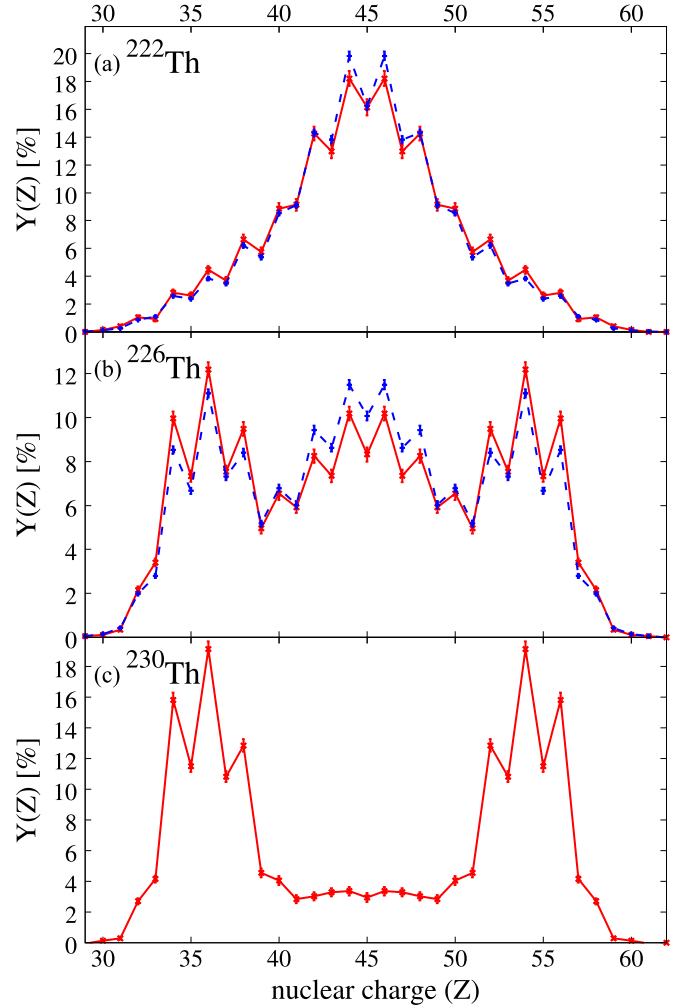


FIG. 10. Comparison of the elemental yields for the thorium isotopes measured in this work (red full lines) and those from Ref. [1] (blue dashed line).

observed, especially for the yields in the symmetric region, where our yields are systematically below the data from Ref. [1]. This is particularly true for the neutron-rich isotopes, for which the nuclear reaction subtraction is important. This feature can be explained. In the previous experiment, the nuclear contribution was evaluated using fission reactions in a plastic scintillator  $(\text{C}_9\text{H}_{10})_n$ , whereas in our case, we avoided all fission sources containing hydrogen. The problem is that for fission reactions induced by hydrogen, the weak factorization principle cannot be rigorously exploited since the limiting fragmentation regime [23] is not reached for the given beam energies. This induces a slight bias of the nuclear background evaluation in Ref. [1]. Moreover, our measurement has a higher charge resolution. Thus the condition  $Z_{\text{sum}} = Z_{\text{CN}}$  is more efficient whereas in the previous data, some events from the tails of  $Z_{\text{sum}} = Z_{\text{CN}} - 1$ , with higher excitation energies, may have been included into the analysis. The symmetric mode was thus overestimated. The full set of elemental yields are given in Fig. 17 of Appendix A.

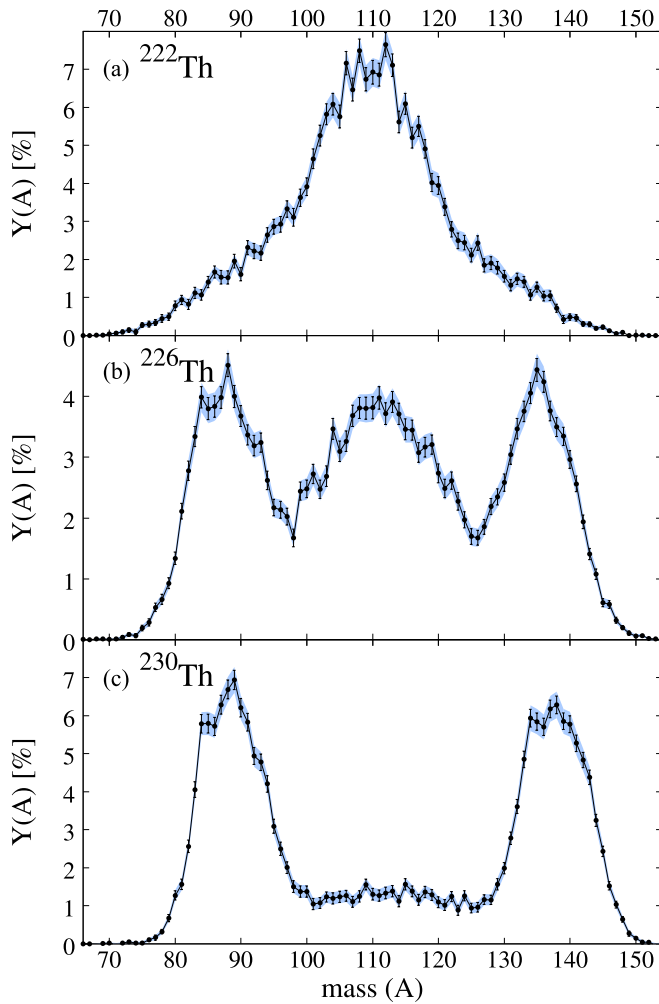


FIG. 11. Isobaric yields for the thorium isotopes with statistical errors (vertical black lines) and systematic uncertainties (blue shaded areas) due to the fit procedure.

### B. Isotonic and isobaric yields

Figures 11 and 12 show the results for the isobaric and isotonic yields for the three most populated secondary beams ( $^{222,226,230}\text{Th}$ ). The full set of data is given in Fig. 20 of Appendix A. The error bars represent the statistical uncertainties propagated along the full analysis. They take into account the nuclear subtraction and the efficiency correction. The additional uncertainties are mainly caused by the gradual loss of resolution. They are estimated from the fit procedure and are represented with the blue shaded areas. For the resolved part of the spectra, they are close to the statistical uncertainties, and they increase for heavier masses.

A neutron even-odd staggering clearly appears in the case of  $^{226}\text{Th}(\gamma, f)$  for which the statistical uncertainties are rather small, and of course only within the range where the isotonic distribution is well resolved ( $N < 70$ ). For the rest of the data, the uncertainties are too large to allow the determination of the even-odd staggering. Moreover, an increase of the production of the fission fragments around the magic numbers  $N = 50$

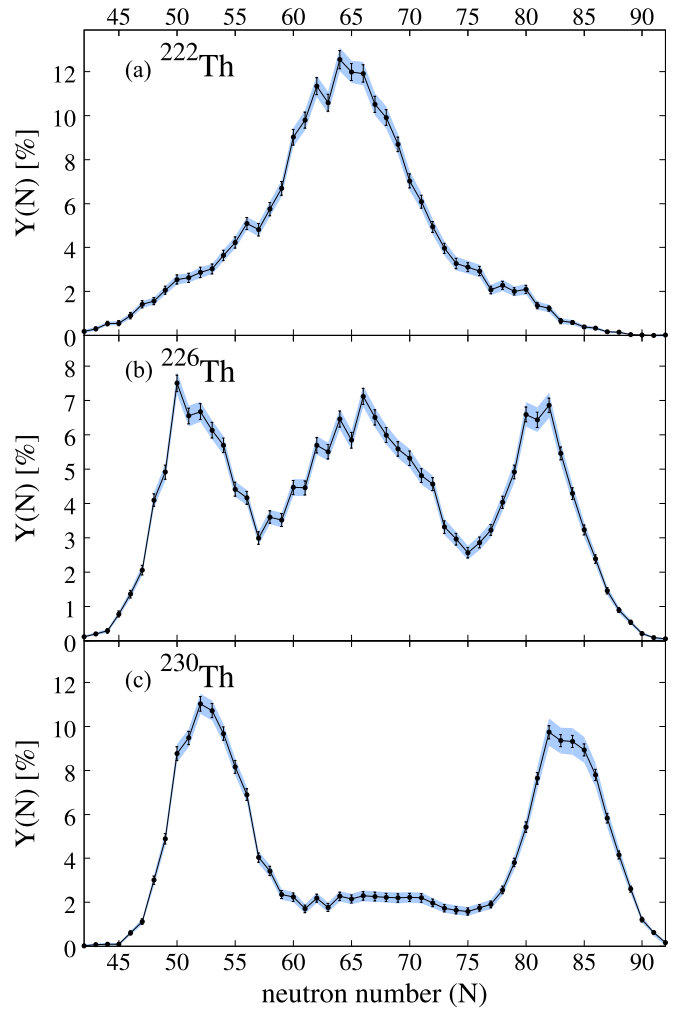


FIG. 12. Isotonic yields for the thorium isotopes with statistical errors (vertical black lines) and the systematic uncertainties (blue shaded areas) due to the fit procedure.

and  $N = 82$  is seen in this favored case of  $^{226}\text{Th}$ , but also for  $^{229,230}\text{Th}$ , where fission is mainly asymmetric. Since the isotonic yields are measured after the neutron evaporation, the spherical shell gaps certainly act like traps during prompt-neutron evaporation. This effect at  $N = 82$  is expected and gives a strong level of confidence in the data for the heavier fission fragments, despite the resolution loss.

### C. Comparison of $^{230}\text{Th}(\gamma, f)$ with $^{229}\text{Th}(n_{th}, f)$

Our data obtained for  $^{230}\text{Th}$  can be compared to previous measurements based on thermal-neutron induced fission of  $^{229}\text{Th}$  [10,11] performed at the Institut Laue Langevin (ILL-Grenoble, France). Both reactions,  $^{230}\text{Th}(\gamma, f)$  and  $^{229}\text{Th}(n_{th}, f)$ , lead to the same compound nucleus but populate different excitation energies. As previously mentioned, in our data, the excitation energy is, on average, around 14.5 MeV, which is about 8 MeV higher than that for the thermal-neutron induced fission, where the  $^{230}\text{Th}$  fissioning nucleus has an excitation energy of 6.8 MeV. Figures 13

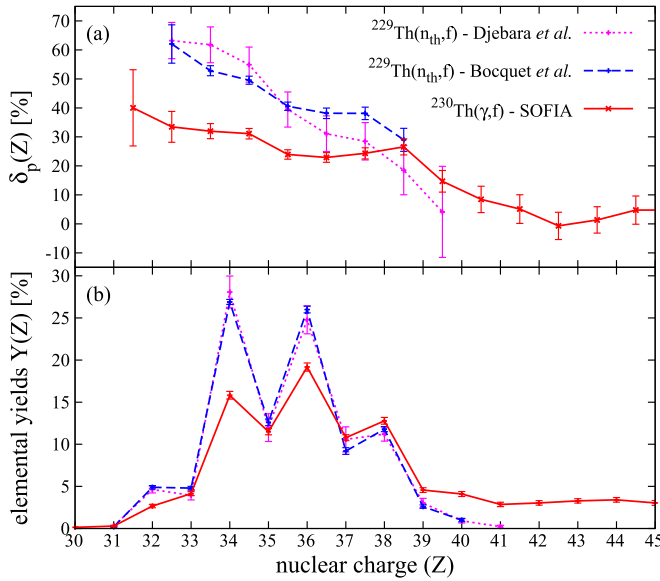


FIG. 13. Comparison of the local even-odd staggering (a) and elemental yields (b) for the fission of the  $^{230}\text{Th}$  fissioning nucleus. Represented by a red full line,  $^{230}\text{Th}$  is populated via the  $(\gamma, f)$  reaction in inverse kinematics (this work). The purple dotted [10] and blue dashed lines [11], represent fission of  $^{230}\text{Th}$  populated by the  $^{229}\text{Th}(n_{th}, f)$  reaction in direct kinematics.

and 14 show the comparison between the different data sets for the elemental yields with the local even-odd staggering (as defined in Ref. [24]) and for the isobaric yields, respectively. The additional 8 MeV of excitation energy of the fissioning nucleus has two expected effects. First, the symmetric valley in the elemental and isobaric yields is more likely to be populated and second, the magnitude of the local even-odd staggering becomes smaller. This feature has already been observed in the heavy actinide region, for which the symmetric fission mode has been interpreted as a superlong mode (SL, as explained in Refs. [25–27]). This SL mode, characterized by

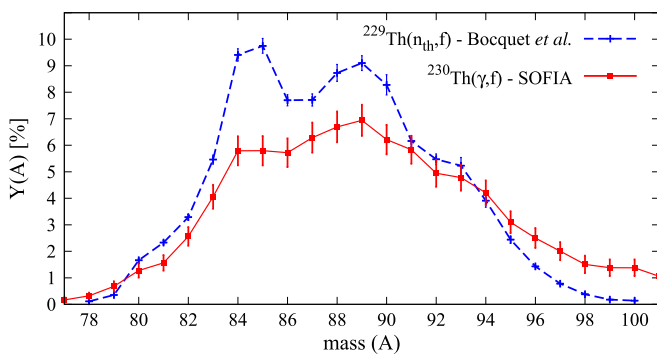


FIG. 14. Comparison of isobaric yields for the fission of the  $^{230}\text{Th}$  fissioning nucleus. For red full line,  $^{230}\text{Th}$  is populated by the  $(\gamma, f)$  reaction in inverse kinematics (this work). For blue dashed line [11],  $^{230}\text{Th}$  is populated by the  $^{229}\text{Th}(n_{th}, f)$  reaction in direct kinematics.

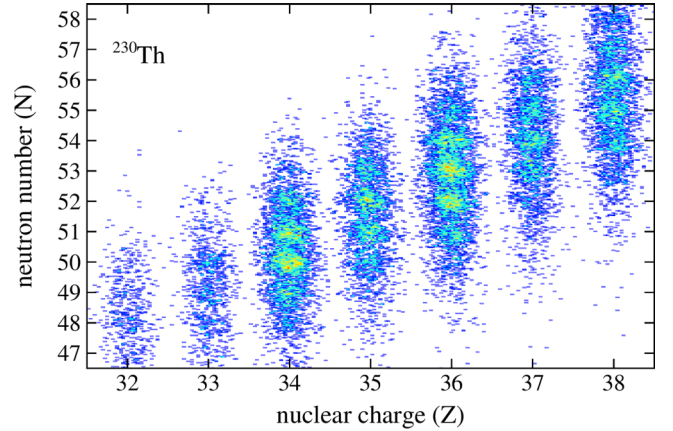


FIG. 15. Isotopic distribution of the light fission fragments produced in  $^{230}\text{Th}(\gamma, f)$ .

two highly deformed symmetric fission-fragments at scission, becomes more and more important as the excitation energy increases and structure effects, such as shell closure or pairing, wash out.

The data of Djebara *et al.* [10] exhibit a steeper decrease of the even-odd staggering with the nuclear charge. This is certainly due to the lower precision of the data, which becomes more of a problem as the nuclear charge of the fission fragments increases. The comparison with the data of Bocquet *et al.* [11] is particularly interesting. They provide the most accurate measurement in direct kinematics. First, compared to this direct-kinematics measurement, the local even-odd effect measured in our experiment is reduced to 35–40 %, but its evolution is rather similar, except for the last point, which corresponds to the limit of the resolution in the direct kinematics data around  $Z = 40$ . Second, the isobaric yields exhibit the same fine structure with the enhancement of the masses  $A = 80$ ,  $A = 84$ ,  $A = 89$ , and  $A = 93$ – $94$ . By plotting the isotopic distribution versus the elemental one (see Fig. 15), we can see that these maxima are mainly populated by fragments around  $(Z = 32, N = 48)$ ,  $(Z = 34, N = 50)$ ,  $(Z = 36, N = 53)$ , and  $(Z = 38, N = 55$ – $56)$ , respectively, and therefore reflects, first the even-odd staggering in  $Z$ , which is of course weaker but still remains in our data, and second the stabilization by the octupole deformation of the heavy partner around  $Z = 52$  to  $Z = 56$  as recently pointed out in Ref. [28].

## V. CONCLUSION

The experimental study along the thorium isotopic chain was first initiated in the 1990s [1], using Coulomb-induced fission in inverse kinematics at relativistic energies. From that experiment, elemental yields were measured, showing a regular transition from asymmetric fission in the heavier thorium isotopes to symmetric fission in the lighter ones. In this article, we report on new data on fission along the thorium isotopic

chain, using the same reaction mechanism, but with the new R3B/SOFIA experimental setup which was conceived to identify the mass and the nuclear charge of the fissioning nuclei and both fission fragments. For the first time, the elemental yields were measured together with the isobaric and isotonic yields, for a broad range of fissioning thorium nuclides.

The agreement between both sets of elemental yields is excellent, and the minor discrepancies have been explained (see Sec. IV A). The isotonic yields show the influence of the closed neutron shells at  $N = 50$  and  $N = 82$ , mainly in the heavier thorium isotopes studied in this experiment ( $^{226,229,230}\text{Th}$ ).

A comparison is done between our measurement of Coulomb-induced fission of  $^{230}\text{Th}$  and previous measurements in direct kinematics of thermal-neutron induced fission of  $^{229}\text{Th}$  [10,11]. Both reaction mechanisms lead to the same compound nucleus but at two different excitation energies. In our experiment, the  $^{230}\text{Th}$  isotope is populated with an additional excitation energy of around 8 MeV. The comparison of the elemental and isobaric yields shows that the asymmetric peak is less populated in comparison with symmetric fission if the system has a larger excitation energy. The comparison of the even-odd staggering indicates that the influence of proton pairing is 35 to 40 % smaller. But still the fine structure remains, e.g., in the isobaric yields. This proves that the structure effects are only partially washed out even with an additional 8 MeV of excitation energy.

#### ACKNOWLEDGMENTS

This work was supported by the GSI/IN2P3-CNRS collaboration Agreement No. 04-48. E.C. is supported by the Spanish Ministry Project No. FPA2010-22174-C02. J.L.R.-S. also acknowledges the support of the European Commission under Project No. ANDES-FP7-249671. We would like to thank the CEA's nuclear energy division for its financial support. K.-H. Schmidt is warmly thanked for the useful discussions, careful reading, and his work on GEF which allows us, in particular, to have reliable fission probabilities.

#### APPENDIX A: FULL SET OF DATA

All results are presented at their last step of analysis, i.e., after the full nuclear subtraction procedure and efficiency correction. Figures 16, 18, and 19 show the elemental, isobaric, and isotonic distributions, respectively. Elemental yields are presented in Fig. 17. Isobaric and isotonic yields are shown on the left and right columns of Fig. 20, respectively.

#### APPENDIX B: SECONDARY BEAMS

Table II gives the statistics for the elemental distributions of the different fissioning nuclei we have reported in this

TABLE II. For each secondary beam listed in column 1, the number of fissions with both fission fragments identified in nuclear charge is given for the events when the fission takes place in the cathodes, anodes, or the TUM-MUSIC window (column 2) and for Coulex-induced fission only, after nuclear subtraction (column 3). The column labeled nuclear weight in the  $Z_{\text{sum}}$  indicates the percentage of fragmentation reactions followed by fission, in which no protons are removed during the fragmentation phase. The last column gives the global efficiency for each secondary beam.

beam	number of events		nuclear weight in the $Z_{\text{sum}}$ [%]	efficiency [%]
	all fissions	coulex		
$^{219}\text{Ac}$	10760	1800	39	$58.0 \pm 1.1$
$^{220}\text{Ac}$	7600	1330	38	$57.9 \pm 1.1$
$^{223}\text{Ac}$	16620	2150	48	$57.6 \pm 0.8$
$^{227}\text{Ac}$	18490	1970	50.5	$53.4 \pm 0.8$
$^{221}\text{Th}$	13990	6510	16	$58.1 \pm 0.4$
$^{222}\text{Th}$	35330	15490	18	$57.5 \pm 0.4$
$^{223}\text{Th}$	7100	3060	17	$56.6 \pm 0.4$
$^{225}\text{Th}$	17980	7100	20	$54.7 \pm 0.3$
$^{226}\text{Th}$	80470	27950	23	$53.3 \pm 0.2$
$^{229}\text{Th}$	26970	8940	25	$49.2 \pm 0.3$
$^{230}\text{Th}$	76200	22430	28	$48.7 \pm 0.3$
$^{228}\text{Pa}$	15810	8230	14	$50.7 \pm 0.4$
$^{229}\text{Pa}$	4580	2140	20	$49.9 \pm 0.4$

work. Approximately 3% of these events are lost during the mass analysis. It requires, for each nuclear charge, additional calibration procedures of the ToF wall, plastic per plastic. The events from the plastics located on the edge at the spatial distribution are lost since the statistics was too small to calibrate them properly. Then, the percentage of the nuclear subtraction is given. It is more and more important for fissioning isotopes exhibiting a lower fission probability. Indeed, the nuclear reaction probability is stable over the range of studied fissioning nuclei, contrary to the probability for electromagnetic-induced fission.

Finally, the last column indicates the global efficiency for each of the secondary beams. Compared to Ref. [8] which reports on a  $^{238}\text{U}(\gamma, f)$  measurement with an efficiency of 63%, we have the same three sources of efficiency loss. However, the global efficiency for the thorium settings is smaller, from 50 to 58 % depending on the fissioning nucleus. This is due to two additional sources of data loss. First, the eighth plastic of the time-of-flight wall was not working, and second, fission fragments are lighter and then more deflected by ALADIN. We nevertheless chose not to change the magnetic field to avoid a full recalibration of the time-of-flight wall. Therefore part of the fission fragments were not detected by the MWPC2 and the time-of-flight wall downstream the magnet.

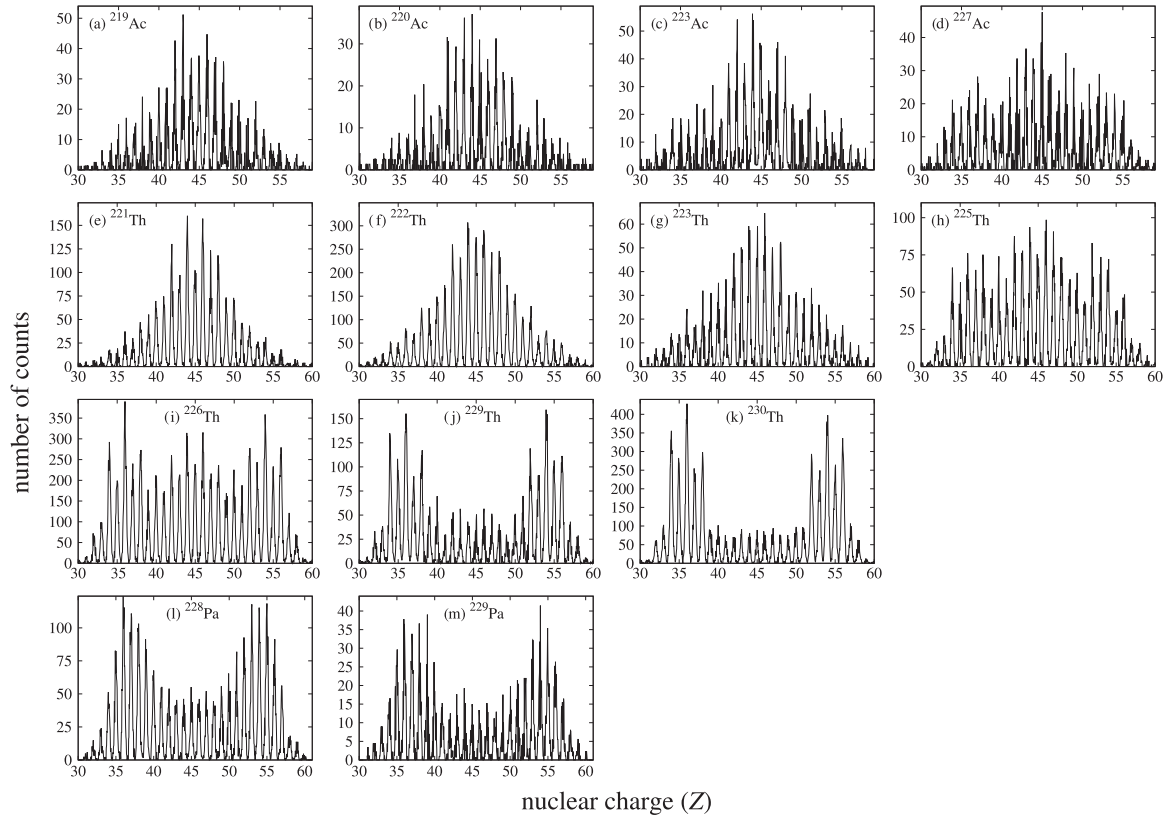


FIG. 16. Measured elemental distributions of the fission fragments from electromagnetic-induced fission of  $^{219,220,223,227}\text{Ac}$ ,  $^{221,222,223,225,226,229,230}\text{Th}$ , and  $^{228,229}\text{Pa}$ .

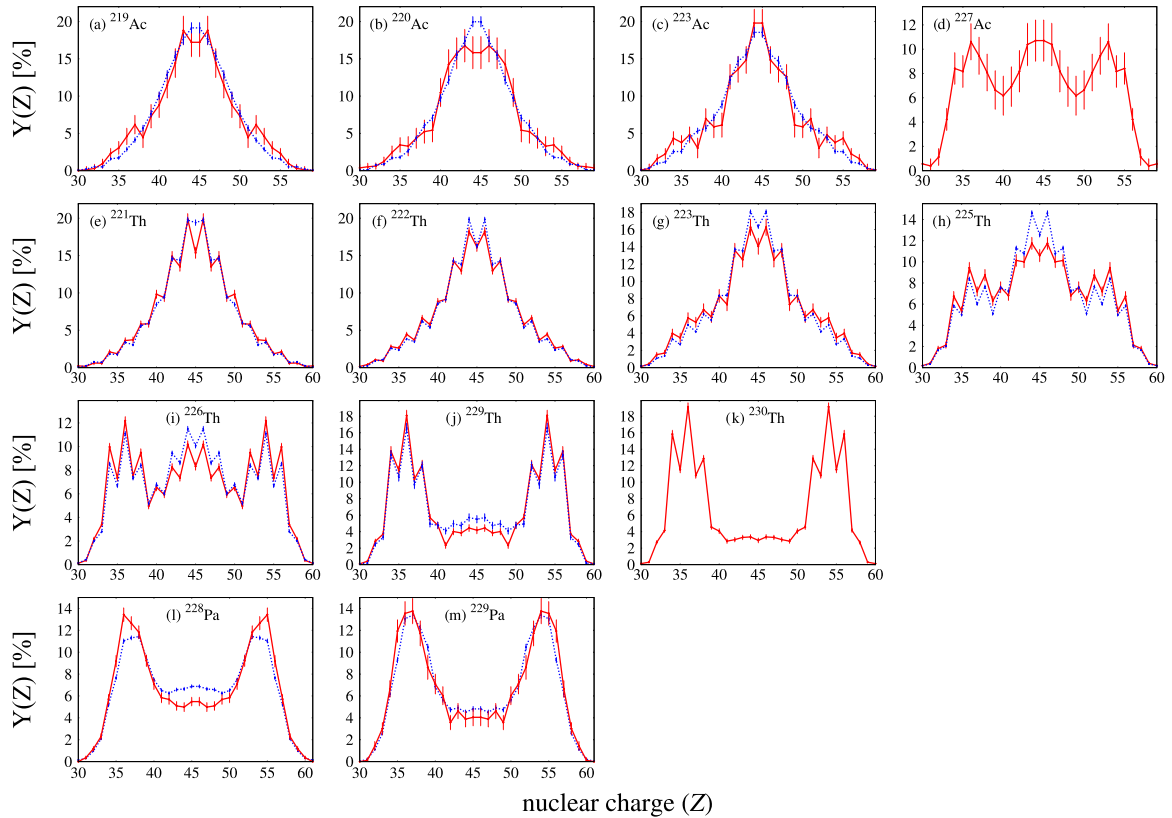


FIG. 17. Comparison of the elemental yields measured in this work (in red) and in Ref. [1] (in blue dotted line).

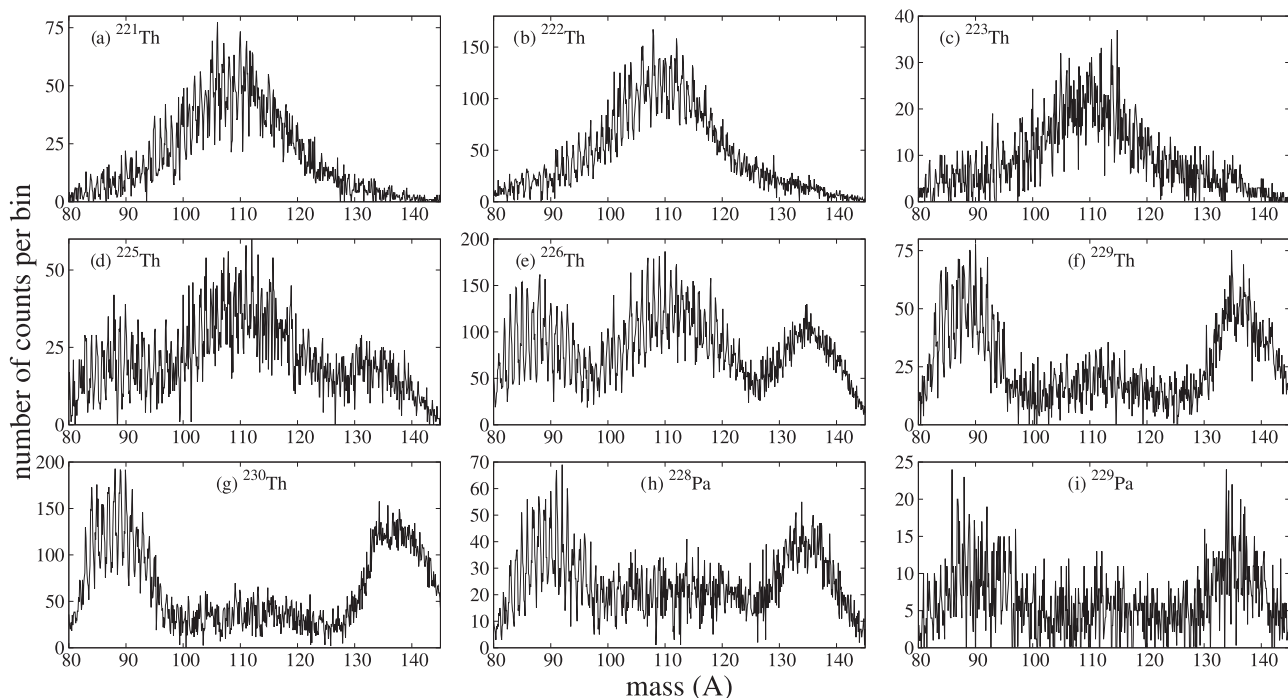


FIG. 18. Measured isobaric distributions of the fission fragments from electromagnetic-induced fission of  $^{221,222,223,225,226,229,230}\text{Th}$  and  $^{228,229}\text{Pa}$ .

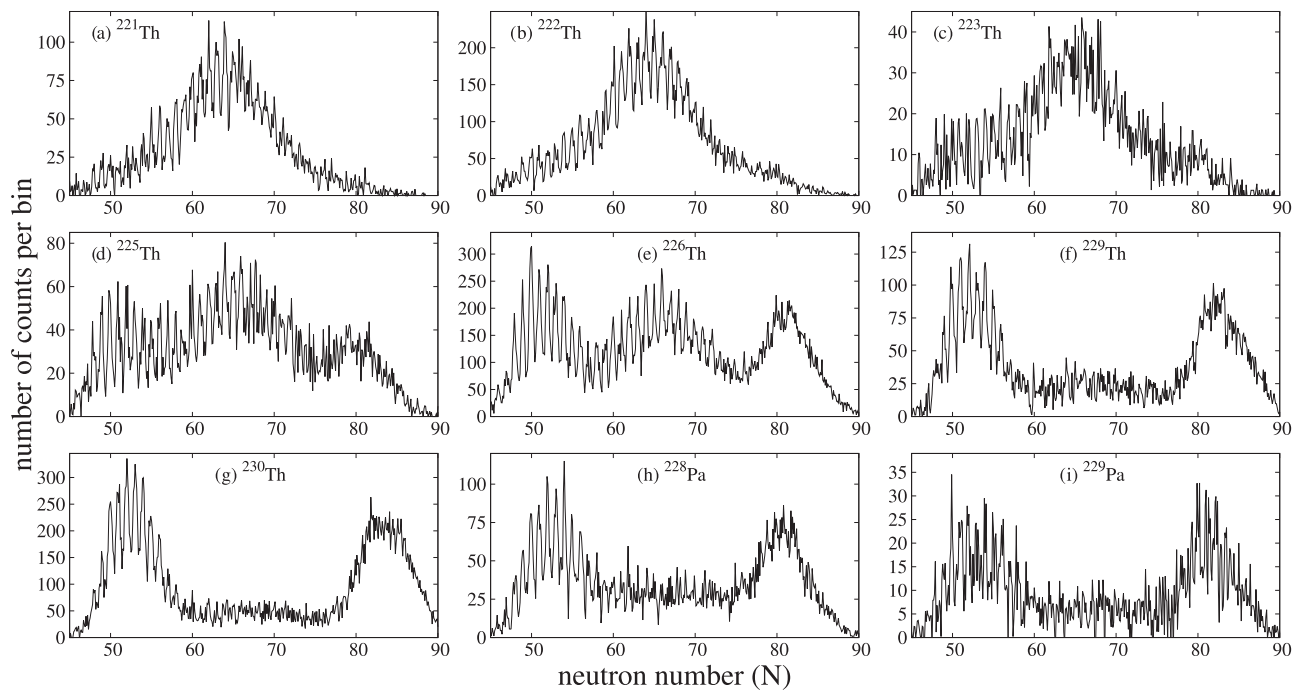


FIG. 19. Measured isotonic distributions of the fission fragments from electromagnetic-induced fission of  $^{221,222,223,225,226,229,230}\text{Th}$  and  $^{228,229}\text{Pa}$ .

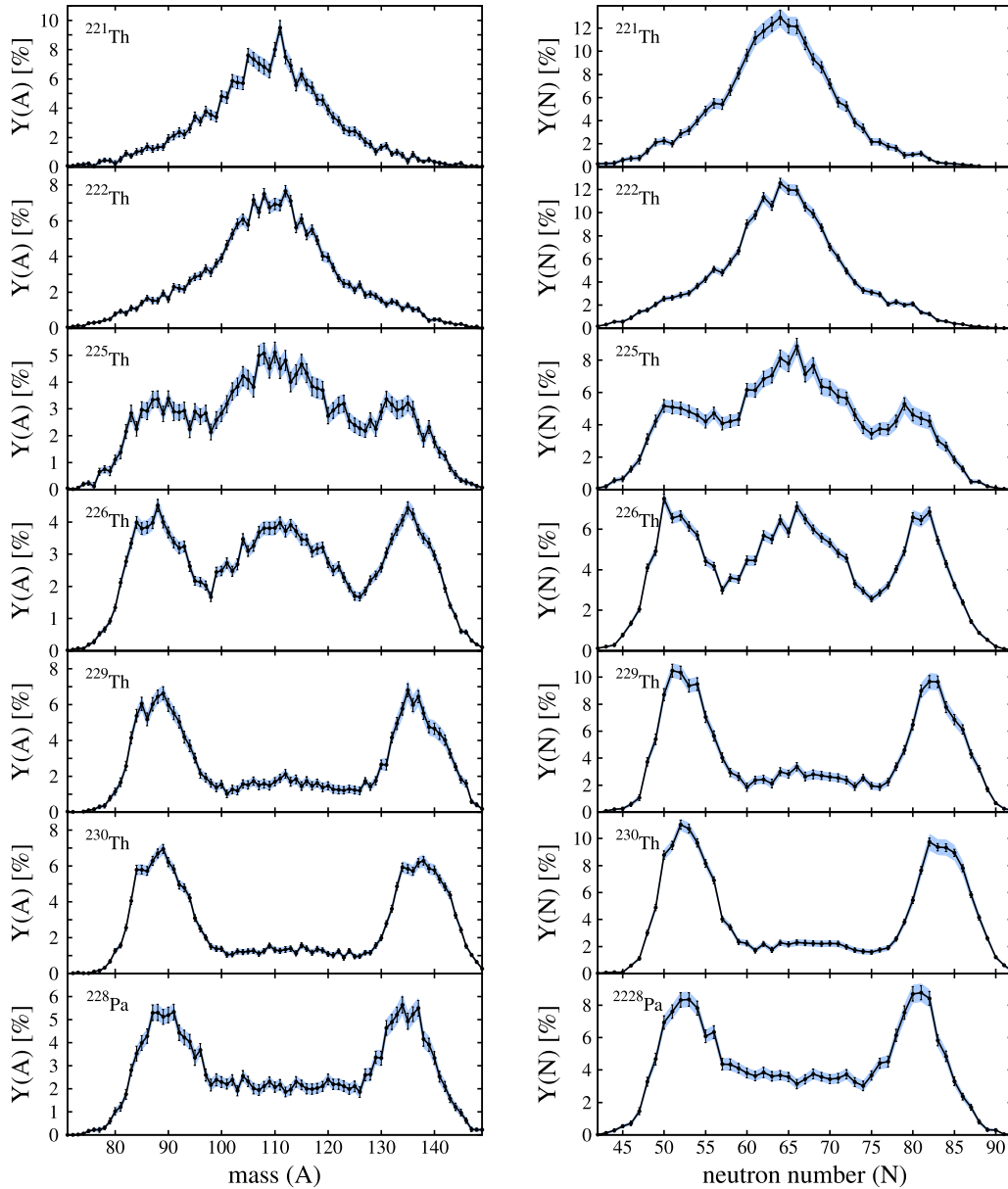


FIG. 20. Isobaric yields (left column) and isotonic yields (right column) for the  $^{221,222,225,226,229,230}\text{Th}$  and  $^{228}\text{Pa}$  isotopes with the statistical error bars (black error bars) and the systematic uncertainty (light blue interval) due to the fit procedure.

- 
- [1] K.-H. Schmidt, S. Steinhäuser *et al.*, *Nucl. Phys. A* **665**, 221 (2000).
- [2] A. N. Andreyev, J. Elseviers, M. Huyse, P. Van Duppen *et al.*, *Phys. Rev. Lett.* **105**, 252502 (2010).
- [3] A. N. Andreyev, M. Huyse, and P. Van Duppen, *Rev. Mod. Phys.* **85**, 1541 (2013).
- [4] N. Boucheneb *et al.*, *Nucl. Phys. A* **502**, 261c (1989).
- [5] A. Bail, O. Serot, L. Mathieu, O. Litaize, T. Materna, U. Köster, H. Faust, A. Letourneau, and S. Panebianco, *Phys. Rev. C* **84**, 034605 (2011).
- [6] M. Caamaño, O. Delaune, F. Farget, X. Derkx, K.-H. Schmidt *et al.*, *Phys. Rev. C* **88**, 024605 (2013).
- [7] J.-F. Martin, J. Taieb, A. Chatillon *et al.*, *Eur. Phys. J A* **51**, 174 (2015).
- [8] E. Pellereau, J. Taieb, A. Chatillon *et al.*, *Phys. Rev. C* **95**, 054603 (2017).
- [9] J. L. Rodríguez-Sánchez, J. Benlliure, J. Taieb *et al.*, *Phys. Rev. C* **91**, 064616 (2015).
- [10] M. Djebara, M. Asghar, J. P. Bocquet, R. Brissot, M. Maurel, H. Nifenecker, and Ch. Ristori, *Nucl. Phys. A* **425**, 120 (1984).
- [11] J. P. Bocquet, R. Brissot, H. R. Faust, M. Fowler, J. Wilhelmy, M. Asghar, and M. Djebara, *Z. Phys. A - Atomic Nuclei* **335**, 41 (1990).

- [12] The ALADIN Collaboration, GSI Scientific Report 1988, GSI 89-1, 292 (1989).
- [13] H. Geissel *et al.*, *Nucl. Instrum. Methods Phys. Res. B* **70**, 286 (1992).
- [14] K.-H. Schmidt *et al.*, *Nucl. Instrum. Methods Phys. Res. A* **260**, 287 (1987).
- [15] J. Jannik *et al.*, *Nucl. Instrum. Methods Phys. Res. A* **640**, 54 (2011).
- [16] W. B. Christie *et al.*, *Nucl. Instrum. Methods Phys. Res. A* **255**, 466 (1987).
- [17] [lise.nscl.msu.edu/lise.html](http://lise.nscl.msu.edu/lise.html).
- [18] K.-H. Schmidt, *Nucl. Data Sheets* **131**, 107 (2016).
- [19] J. T. Caldwell, E. J. Dowdy, B. L. Berman, R. A. Alvarez, and P. Meyer, *Phys. Rev. C* **21**, 1215 (1980).
- [20] ALICE Collaboration, *J. Phys. G: Nucl. Part. Phys.* **30**, 1517 (2004).
- [21] A. Ebran, J. Taieb, G. Belier, A. Chatillon, B. Laurent, J.-F. Martin, and E. Pellereau, *Nucl. Instrum. Methods Phys. Res. A* **728**, 40 (2013).
- [22] <http://www.khs-erzhausen.de/CONFID.html>.
- [23] J. R. Cummings, W. R. Binns, T. L. Garrard, M. H. Israel, J. Klarmann, E. C. Stone, and C. J. Waddington, *Phys. Rev. C* **42**, 2530 (1990).
- [24] B. L. Tracy, J. Chaumont, R. Klapisch, J. M. Nitschke, A. M. Poskanzer, E. Roeckl, and C. Thibault, *Phys. Rev. C* **5**, 222 (1972).
- [25] U. Brosa, *Phys. Rev. C* **38**, 1944 (1988).
- [26] F.-J. Hambsch, H.-H. Knitter, and C. Budtz-Jørgensen, *Nucl. Phys. A* **491**, 56 (1989).
- [27] U. Brosa, S. Grossmann, and A. Müller, *Phys. Rep.* **197**, 167 (1990).
- [28] G. Scamps and C. Simenel, *Nature* **564**, 382 (2018).